

Strain-induced nuclear quadrupole splittings in silicon devices

J.J. Pla,¹ A. Bienfait,² G. Pica,^{3,*} J. Mansir,⁴ F.A. Mohiyaddin,¹ A. Morello,¹ T. Schenkel,⁵ B.W. Lovett,³ J.J.L. Morton,⁴ and P. Bertet²

¹*School of Electrical Engineering and Telecommunications,
University of New South Wales, Anzac Parade, Sydney, NSW 2052, Australia*

²*Quantronics Group, SPEC, CEA, CNRS, Université Paris-Saclay, CEA-Saclay, 91191 Gif-sur-Yvette, France*

³*SUPA, School of Physics and Astronomy, University of St Andrews, KY16 9SS, United Kingdom*

⁴*London Centre for Nanotechnology, University College London,
17-19 Gordon Street, London, WC1H 0AH, United Kingdom*

⁵*Accelerator Technology and Applied Physics Division,
Lawrence Berkeley National Laboratory, Berkeley, California 94720, USA*

(Dated: August 29, 2016)

In spin-based quantum information processing devices, the presence of control and detection circuitry can change the local environment of a spin by introducing strain and electric fields, altering its resonant frequencies. These resonance shifts can be large compared to intrinsic spin line-widths and it is therefore important to study, understand and model such effects in order to better predict device performance. Here we investigate a sample of bismuth donor spins implanted in a silicon chip, on top of which a superconducting aluminium micro-resonator has been fabricated. The on-chip resonator provides two functions: first, it produces local strain in the silicon due to the thermal contraction of the aluminium, and second, it enables sensitive electron spin resonance spectroscopy of donors close to the surface that experience this strain. Through finite-element strain simulations and effective mass theory calculations of the donor electron wavefunction, we are able to reconstruct key features of our experiments, including the electron spin resonance spectra. Our results reveal a large strain-induced quadrupole interaction in the bismuth donors, of order 100 MHz.

The spins of dopant atoms in silicon devices have been shown to have great promise for quantum information processing (QIP) [1–5]. This has, in part, been encouraged by the extraordinarily long spin coherence times demonstrated, surpassing 1 second for the electron spin [6] and 3 hours for the nuclear spin [7] of the phosphorus (³¹P) donor. Experiments that detect and control individual ³¹P electron and nuclear spins with nanoelectronic circuits [8] have demonstrated the importance of considering the effect of such structures on the local environment of the spin. For example, it was shown that the electric fields produced in these devices can shift the spin resonance frequencies up to four orders of magnitude more than the intrinsic line-width when the donor is hosted in an isotopically enriched silicon substrate [9].

Another donor in silicon with considerable promise for QIP is bismuth (²⁰⁹Bi). Its large nuclear spin $I = 9/2$ and hyperfine constant $A = 1475$ MHz (which describes the interaction between the electron \mathbf{S} and nuclear \mathbf{I} spins $A\mathbf{S} \cdot \mathbf{I}$) provides rich features such as decoherence-suppressing atomic-clock transitions [10–12], where coherence times can exceed by two orders of magnitude those typically achieved using other donor species. The Si:Bi system also possesses a large zero-field splitting of 7.375 GHz, making it an attractive dopant for use in hybrid superconducting devices [13, 14] such as quantum memories [15–18].

For the heavier donors in silicon (arsenic, antimony and bismuth), little work has been done on studying their spin resonance spectra in close proximity to micro- or nanoelectronic devices. Recently, it was reported that the

presence of charge defects at the Si/SiO₂ interface could induce shifts on the nuclear magnetic resonance (NMR) frequencies of these dopants through a quadrupole interaction [19]. Strain is known to also play an important role in determining the nuclear spin resonances of the heavier donors — for example, it has been demonstrated that a uniformly applied strain can impart quadrupole shifts on the NMR lines of arsenic-doped silicon samples [20, 21].

Strain is an inherent feature of metal-oxide-semiconductor (MOS) electronic devices and results from a mismatch of the coefficient of thermal expansion (CTE) of the various composing materials [22, 23]. It is therefore crucial to understand and predict the effect of intrinsic device strains on donors such as bismuth, as this can aid the design of scalable donor-based QIP and hybrid superconducting device architectures, serving as a guide to the often expensive and time-consuming fabrication process. Here we study a sample of ²⁰⁹Bi donors implanted 75 nm beneath a thin-film aluminium wire (Figs. 1a and b). We find that strain induced by the surface aluminium structure substantially alters the spin resonance spectra of the bismuth donors. A model is developed that is able to reproduce many facets of our measurements, demonstrating the ability to predict device behavior and illustrating the importance of considering strain in semiconductor micro and nanoelectronic quantum devices.

Our device (Fig. 1a) consists of two superconducting aluminium microwave resonators patterned on the surface of a bismuth-doped isotopically-enriched silicon sub-

strate. The resonators are a lumped-element design, they contain a central inductive wire that produces an oscillating microwave magnetic field B_1 to drive and detect spin resonance. The drive field B_1 is directly proportional to the magnetic vacuum fluctuations δB_1 in the resonator, a quantity that we can simulate directly for our device. We utilize δB_1 in the following calculations and discussion: it is readily determined from our simulations (unlike B_1 , which requires an accurate calibration of losses and other experimental parameters), and as we mention below, it provides us with another important measure, the spin-resonator coupling strength g . A simulation of δB_1 is performed knowing only the impedance of the resonator Z_0 and its frequency $\omega_0/2\pi$, and by calculating the resulting vacuum current fluctuations $\delta i = \omega_0 \sqrt{\hbar/(2Z_0)}$ in the wire (where \hbar is the reduced Planck's constant). The current density distribution in the superconducting film (depicted in Fig. 1c) is evaluated [24] and fed into a finite-element magnetostatic solver (COMSOL Multiphysics), with the resulting $|\delta B_1|$ profile shown in Fig. 1d. We observe a strong spatial dependence of the δB_1 orientation at the donor implantation depth (Fig. 1e). Underneath the wire, the Y component of the field δB_{1Y} dominates, whilst to the side δB_{1Z} is the largest. We utilize this trait later in order to study spins in different spatial regions through orientation-dependent electron spin resonance (ESR) spectroscopy [13, 25, 26].

A static magnetic field B_0 is applied in the plane of the aluminium resonators, with a variable angle ϕ relative to the inductive wire. This field allows us to fine-tune the spin transition frequencies of the ^{209}Bi donors. At values of the magnetic field where the electron Zeeman frequency $E_z/\hbar = \gamma_e B_0 \lesssim A$ ($\gamma_e = 28 \text{ GHz/T}$ being the electron gyromagnetic ratio), the eigenstates become strongly mixed in the electron-nuclear spin basis and are best described by the total spin $\mathbf{F} = \mathbf{I} + \mathbf{S}$ and its projection onto B_0 , m_F [10]. We chose the frequencies of the resonators to be close to the Si:Bi zero-field splitting of 7.375 GHz in order to minimize field-induced losses in the superconducting films, achieving $\omega_{0A}/2\pi = 7.305 \text{ GHz}$ for resonator A and $\omega_{0B}/2\pi = 7.248 \text{ GHz}$ for resonator B. We therefore operate in the regime where F and m_F are good quantum numbers and we describe states in the $|F, m_F\rangle$ basis. The device is mounted inside a dilution refrigerator with a base temperature of 20 mK. We are able to detect the spin echo signals produced by the small number of shallow-implanted donors underneath each wire (estimated at $\sim 10^7$) by utilizing a quantum-noise-limited ESR setup, as described in Refs. [13, 25].

First, we observe the ESR spectrum by performing an echo-detected magnetic field sweep with $B_0 \parallel X$ ($\phi = 0^\circ$), afterwards repeating with the orthogonal orientation $B_0 \parallel Y$ ($\phi = 90^\circ$). A measurement on the lowest-field spin resonance line (Fig. 2a), corresponding to a transition between the states $|4, -4\rangle \leftrightarrow |5, -5\rangle$, is shown in Fig. 2 for resonator B. The spatially-varying mag-

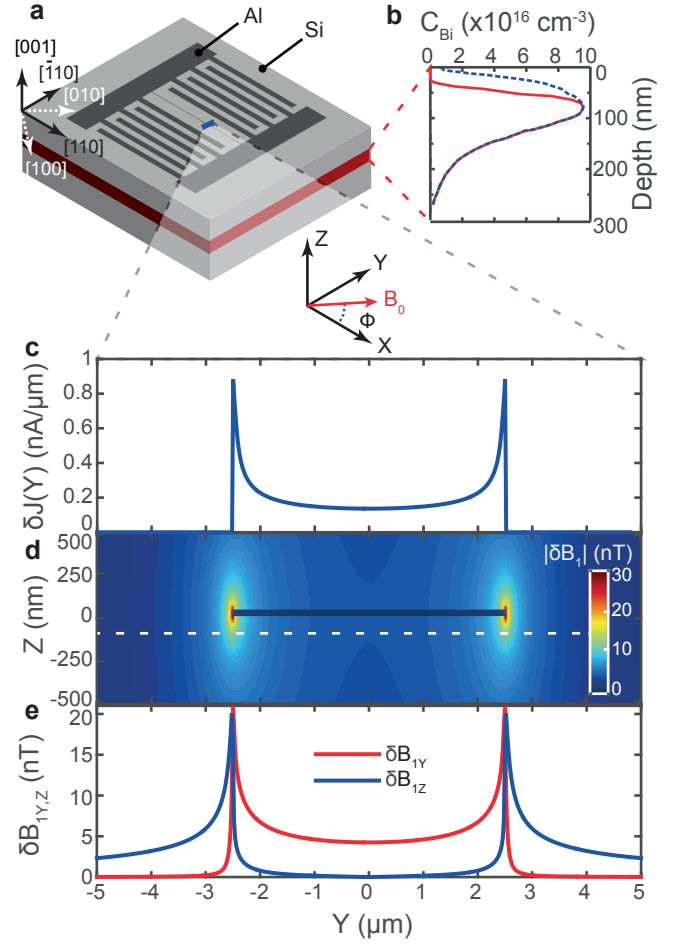


FIG. 1. **a** Sketch of an LC superconducting resonator made from 50 nm thick aluminium, patterned on a silicon substrate, with central inductor 5 μm wide and 700 μm long. The silicon is composed of a 700 nm epitaxial layer of 99.95% enriched ^{28}Si on top of a natural silicon (001) handle wafer. The sample was cleaved along the $\langle 110 \rangle$ crystal axes and we specify a sample frame such that $X \parallel [110]$, $Y \parallel [\bar{1}10]$ and $Z \parallel [001]$. The static field B_0 can be oriented in any direction in the XY-plane with an angle ϕ . **b** Bismuth donor doping profile. The blue dashed curve shows the result of a secondary ion mass spectrometry (SIMS) measurement, whilst the red curve is the result of a finite-element simulation that incorporates the fraction of donors underneath the wire ionized by the Schottky junction between the aluminium and silicon. **c** A calculation of the current density vacuum fluctuations in the wire. Equations describing the current density profile were adapted from Ref. [24]. The only input to this calculation is the impedance of the resonator $Z_0 = 44 \Omega$ and its frequency $\omega_0/2\pi \approx 7.3 \text{ GHz}$, extracted using CST Microwave Studio. **d** A COMSOL Multiphysics finite-element simulation of the spatial dependence of the magnetic field vacuum fluctuations δB_1 magnitude produced by the current density in panel c. **e** Components of δB_1 along the Y and Z axes at a depth of 75 nm (corresponding to the peak donor concentration), marked by the white dashed line in panel d.

tude of δB_1 (Fig. 1d) in our device implies a spatially-

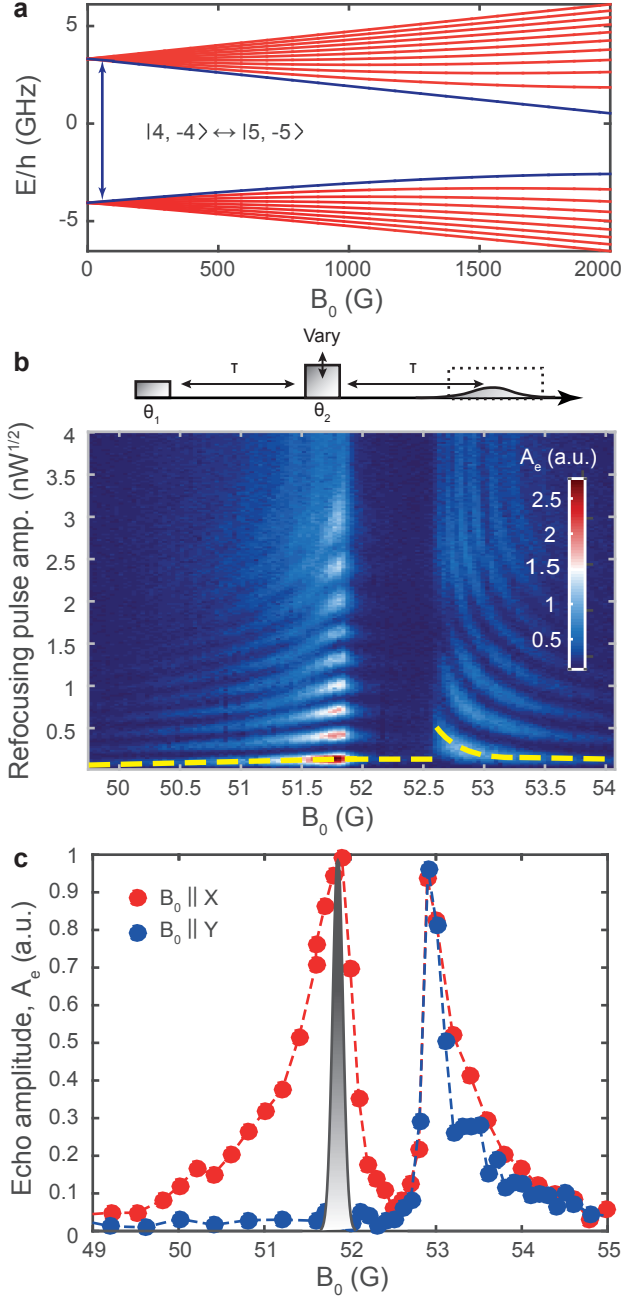


FIG. 2. **a** Eigenstate frequencies of the Si:Bi system. The purple states and arrow identify the $|4, -4\rangle \leftrightarrow |5, -5\rangle$ transition probed in panels b and c. **b** Rabi oscillations as a function of B_0 for the $|4, -4\rangle \leftrightarrow |5, -5\rangle$ transition of resonator B ($\omega_{0B}/2\pi = 7.248$ GHz). The amplitude of the refocusing pulse in a Hahn echo sequence (shown above) is varied to reveal oscillations in the integrated echo signal A_e (marked by the black dashed box in the sequence). **c** A compensated echo-detected field sweep, taken using the calibrated π -pulse amplitudes of panel b (yellow dashed line). The grey gradient-filled curve depicts the expected ESR spectrum, whilst the solid circles show the measured spectra (averaged over 8 sequences with a repetition rate of 0.2 Hz) for different field orientations.

varying spin to resonator coupling strength g , with the two being linked through the relation $g = \gamma_e M |\delta B_{1\perp}|$, where M is the ESR transition matrix element between the two states (see Supplementary Material) and $|\delta B_{1\perp}|$ is the magnitude of the δB_1 component perpendicular to B_0 . Such a variation might be detected experimentally through measuring the Rabi frequency $\Omega_R = 2g\sqrt{\bar{n}}$ (with \bar{n} being the mean intra-cavity photon number, proportional to the input microwave power) as a function of B_0 across the ESR line. In the absence of any inhomogeneous broadening, the different Rabi frequencies would sum to produce a pattern of rapidly decaying oscillations [27, 28]. However, if the presence of the resonator also served to produce a spectral distribution of the spins (for example through generating strain), then it should be possible to correlate segments of the resulting inhomogeneously broadened line with spatial regions in the device through the measurement of the Rabi frequency Ω_R .

We perform such a measurement in Fig. 2b, where we vary the amplitude of the refocusing pulse in a Hahn echo sequence [29], integrate and record the detected echo signal A_e for each pulse amplitude (see depicted pulse sequence), and repeat for different values of B_0 . When the refocusing pulse equals a multiple of π , the integrated spin echo signal is maximized, revealing a series of Rabi oscillations. Remarkably, we find that the Rabi frequency does indeed have a B_0 field dependence, increasing on the tails of the transition, demonstrating a correlation between the Larmor frequency of each spin and its coupling strength to the microwave field. Although the inhomogeneous δB_1 provides a valuable way to assign different components of the observed ESR line to different spatial regions, it is also desirable to obtain the intrinsic ESR line-shape of the ensemble being probed by the resonator (showing peak heights, broadening and any asymmetries). We achieve this by using so-called ‘compensated’ field sweeps (displayed in Fig. 2c), where for each value of B_0 the pulse amplitudes are calibrated (yellow dashed line in Fig. 2b) to give $\pi/2$ and π pulses in the echo sequence.

In the absence of strain, we expect to observe a single resonance peak (gradient-filled curve in Fig. 2c), with a line-width of order 190 mG, as measured on this same sample using a standard inductive ESR spectrometer at X-band and with no planar on-chip resonator [30] (see also Supplementary Material). Instead, we observe that the resonance is split into two, each peak ~ 1 G wide, representing a total broadening greater than an order of magnitude. Comparing the (compensated) echo-detected ESR spectra for the different orientations of B_0 (red and blue circles in Fig. 2c) provides insight into the origin of the resonance splitting and broadening. Here we find that the low-field peak vanishes for $B_0 \parallel Y$ ($\phi = 90^\circ$) while the high-field peak remains relatively unchanged. This can be understood by considering again Fig. 1e. As noted previously, spins underneath the wire experience a

δB_1 field almost entirely along Y , whilst the spins to the side of the wire see a δB_1 field along Z . For the spectrum recorded with $B_0 \parallel X$ ($\phi = 0^\circ$), spins underneath the wire as well as those to the side experience $\delta B_1 \perp B_0$ and therefore contribute to the echo signal at this transition, which obeys the selection rule $\Delta m_F = \pm 1$. However, for the spectrum with $B_0 \parallel Y$ ($\phi = 90^\circ$), resonance is no longer possible at this field for the spins directly below the wire, which experience a $\delta B_1 \parallel B_0$. This indicates that the presence of the inductive wire is the cause of the splitting, and as we demonstrate in this work, it is likely that the underlining mechanism is strain in the silicon resulting from the thermal contraction of the aluminium. We refer the reader to the Supplementary Material for an analysis of other potential mechanisms.

Further evidence in support of this is found by once again considering the field-dependence of the Rabi frequency (Fig. 2b). For the high-field peak in the ESR spectra (originating from spins located to the side of the wire), the sharp transition at the low-field edge likely corresponds to spins far from the wire that do not experience a significant strain distribution and are therefore bulk-like in their behavior. Being far from the wire, these spins also display a reduced Rabi frequency, observed as slower oscillations in Fig. 2b. Moving closer to the wire, the strength of the strain should increase, as does the magnitude of the δB_1 field (see Fig. 1d). We thus anticipate the broadened regions of the lines (the tails) to have an enhanced Rabi frequency, and this is indeed the case.

To better understand these measurements we perform finite-element strain simulations of our aluminium wire on the silicon substrate. We assume the aluminium to be strain-free upon deposition [31, 32] and simulate cooling the device to 20 mK using the temperature-dependent CTEs of the materials and anisotropic stiffness coefficients for silicon. The difference in the CTEs of Si and Al produces device strain at low temperature. Three of the six independent strain tensor components (those along the $\langle 100 \rangle$ crystal axes) are plot in Fig. 3a as a function of position. The full strain tensor and its spatial dependence can be found in the Supplementary Material.

We now provide a more detailed explanation of some mechanisms by which strain may result in a shift of the bismuth spin transition frequencies. Strain can cause a reduction of the hyperfine interaction strength A [33] or modify the electron g-factor g_e , both resulting in a resonance shift. We have performed numerical calculations using the simulated strain profiles and can rule out both of these mechanisms due to the small strength of the effect (see Supplementary Material). Of the two mechanisms, we expect a reduction in A to have the greatest effect on the resonance frequency, shifting it to a lower magnetic field. Importantly, the sign of this shift should not change with the sign of the strain and cannot therefore explain the splitting of the resonance peak. Another mechanism we consider that could produce the required

frequency distribution containing both positive and negative components is the quadrupole interaction (QI).

Nuclei with a spin $I > 1/2$ can have a non-spherical charge distribution and associated with this is a quadrupole moment Q [34]. This charge distribution has an axis of symmetry that aligns with the nuclear angular momentum and interacts with an electric field gradient (EFG) $V_{\alpha\beta}$ (where α and β are principal axes in the local crystal coordinate system) produced by external charges, such as the donor-bound electron. The interaction is described by the following quadrupole Hamiltonian (in frequency units):

$$H_Q = \gamma \frac{eQV_{zz}}{4I(2I-1)\hbar} [3I_z^2 - \mathbf{I}^2 + \eta(I_x^2 - I_y^2)] \quad (1)$$

where γ is a multiplicative scaling factor (discussed in detail below), e is the electron charge, \hbar is Planck's constant, \mathbf{I} is the nuclear spin operator with components I_α , I in the denominator is the scalar value of the nuclear spin ($I = 9/2$) and $\eta = (V_{xx} - V_{yy})/V_{zz}$ is an asymmetry parameter. It is evident from Eq. 1 that the existence of an EFG $V_{\alpha\beta}$ produces a frequency shift between states with different nuclear spin projections m_I . In the case of the Si:Bi spin system at low magnetic fields, the strong mixing of the electron and nuclear spins by the hyperfine interaction is therefore also expected to produce a quadrupole shift of the ESR transitions.

Silicon has a conduction band minimum that is six-fold degenerate along the $\langle 100 \rangle$ equivalent crystallographic directions — commonly referred to as “valleys” [35] (see Fig. 3b). The degeneracy of these valleys is broken by the confining potential of the donor, resulting in a singlet A_1 ground state and doublet E and triplet T_1 excited states [36]. The A_1 ground state of the donor electron comprises an equal combination of Bloch wavefunctions at each of the valleys, providing a high degree of symmetry for this state. Evaluating the EFG tensor components $V_{\alpha\beta} = \langle \psi | \frac{\partial^2 V(\mathbf{r})}{\partial \alpha \partial \beta} | \psi \rangle$, where $V(\mathbf{r})$ is the electrostatic potential produced at the nucleus by the electron charge with a wavefunction $|\psi\rangle$, gives $V_{\alpha\beta} = 0$ for the symmetric case of $|\psi\rangle = |A_1\rangle$ (see Supplementary Material). For a donor in a bulk silicon crystal (in the absence of strain and electric fields) the electron is perfectly described by the singlet ground state $|\psi\rangle = |A_1\rangle$ and the quadrupole interaction is therefore non-existent. It is only through mixing the donor ground state wavefunction with the valley-orbit excited states that a non-vanishing EFG tensor is realized.

In our device, the strain (Fig. 3a) admixes the A_1 ground state with the E doublet excited state [37]. We use effective mass theory (EMT), as developed in Ref. [38], to calculate the strained donor electron wavefunction at each position in the device. An example of the unstrained A_1 wavefunction produced from our EMT

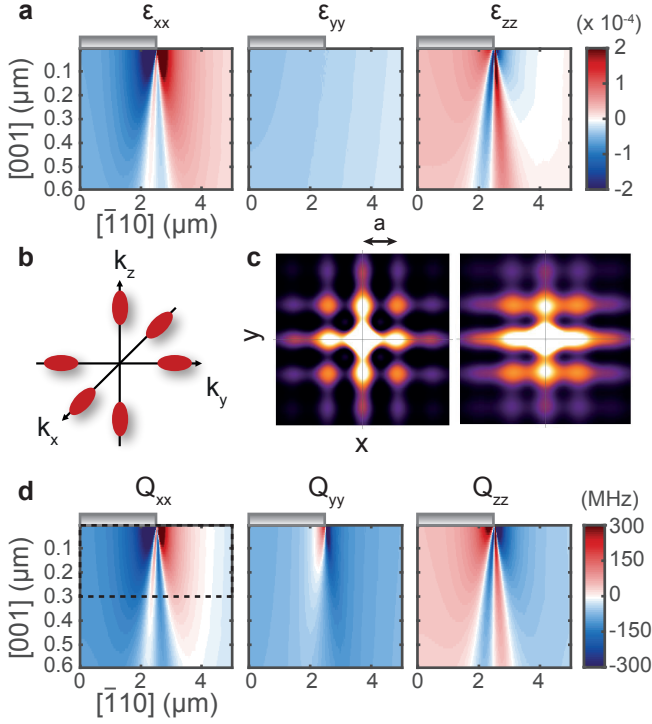


FIG. 3. **a** Finite-element COMSOL simulations of the strain tensor components along the $x \parallel [100]$, $y \parallel [010]$ and $z \parallel [001]$ crystal axes and their variation as a function of position in the device. A cross-section of the aluminium wire (drawn to scale) is represented by the grey gradient-filled box above the silicon substrate (which bounds the strain data). Here the xyz crystal axes are related to the sample frame XYZ (used to describe δB_1 and B_0) by a 45° rotation about Z (see Fig. 1a). We show the result for the wire running parallel to the $[110]$ (or X) axis, the direction in which the sample was cleaved. **b** Momentum-space diagram of the six-fold degenerate conduction band minima, or “valleys”, in bulk silicon. The minima exist 85% of the way to the Brillouin zone boundary. **c** Example of an unstrained (left) and strained (right) donor electron wavefunction calculated using effective mass theory. An amplified strain $\epsilon_{xx} = 0.1$ was used in the calculation in order to aid in illustrating its effect on the wavefunction. Here $a = 0.54$ nm is the silicon lattice constant. **d** Principal components of the quadrupole interaction as a function of position, evaluated from EMT calculations of the strained donor wavefunction using the simulated strain tensor components (partially shown in panel a). The black dashed box in the left-most panel highlights the region in which donors have been implanted.

can be seen in Fig. 3c (left panel). We plot beside this a strained wavefunction where a reduction in symmetry is apparent as the doublet excited state becomes mixed with the ground state. From these strained wavefunctions, we evaluate the EFG components $V_{\alpha\alpha}$ ($\alpha = x, y, z$) — the off-diagonal tensor elements are zero owing to symmetry (see Supplementary Material). The quadrupole tensor components $Q_{\alpha\alpha} = \gamma_e Q V_{\alpha\alpha} / h$ are then calculated and displayed in Fig. 3d. These results show a sizable QI

for donors in the vicinity of the wire, with a magnitude of approximately 100 MHz for strains of order 10^{-4} , producing an equivalent shift of the $|4, -4\rangle \leftrightarrow |5, -5\rangle$ transition of ~ 1 MHz.

To assess the validity of the quadrupole calculations, we perform a full simulation of extended ESR spectra (Fig. 4). In Fig. 4a we plot the low-field ESR transition frequencies and their crossing with resonator A (see Supplementary Material for a full description of these transitions). A measurement of the first three transitions with $B_0 \parallel X$ (obeying the selection rule $\Delta m_F = \pm 1$ for all spins) is shown in the compensated echo-detected field sweep of Fig. 4b (lower red trace) for resonator A. Also presented here is the spectrum recorded with $B_0 \parallel Y$ (lower blue trace), where the selection rule is given by $\Delta m_F = 0$ for spins underneath the wire (as $B_0 \parallel \delta B_1$) and $\Delta m_F = \pm 1$ for spins to the side (since $B_0 \perp \delta B_1$). The first three $\Delta m_F = 0$ transitions are observed, and the lack of a splitting of these peaks strongly supports the claim that they originate from spins underneath the wire (the only region with $B_0 \parallel Y$), where the strain is uni-polar (Fig. 3a). The experiments are repeated for resonator B and displayed in the lower traces of Fig. 4c.

The upper offset traces of Figs. 4b and c are the results of a numerical model incorporating the finite-element simulations and EMT calculations of the QI. For every pixel in the device where dopants are present, we use the quadrupole tensor components calculated for that pixel and simulate a field-sweep by solving the combined spin Hamiltonian:

$$H = \gamma_e \mathbf{B}_0 \cdot \mathbf{S} - \gamma_n \mathbf{B}_0 \cdot \mathbf{I} + \mathbf{A} \mathbf{S} \cdot \mathbf{I} + H'_Q \quad (2)$$

where γ_n is the nuclear gyromagnetic ratio and $\mathbf{B}_0 = B_0 \mathbf{X}$ or $B_0 \mathbf{Y}$ (depending on the measurement being investigated). H'_Q is the quadrupole Hamiltonian of Eq. (1) transformed from the principal axes coordinate system (that aligns with the $\langle 100 \rangle$ silicon crystal axes) to the sample frame (as defined in Fig. 1a). We weight the spectrum from each pixel with the corresponding donor concentration and the strength of the magnetic field vacuum fluctuations (Fig. 1), then sum over all pixels. We note that the donor doping profile used in this model (red solid curve in Fig. 1b) is the output of a finite-element Poisson equation solver (Synopsys TCAD), which takes into account the ionization of donors in the depletion region of the Schottky junction formed between the aluminium wire and the silicon substrate. The resulting spectra reproduce many features in the experimental data, including peak splittings, peak-height asymmetries and field orientation ϕ dependence. There are a few areas in which the model could be improved, for example in describing the $\Delta m_F = 0$ peak positions and asymmetries. We believe that this could be achieved through a more sophisticated strain model, incorporating realistic device prop-

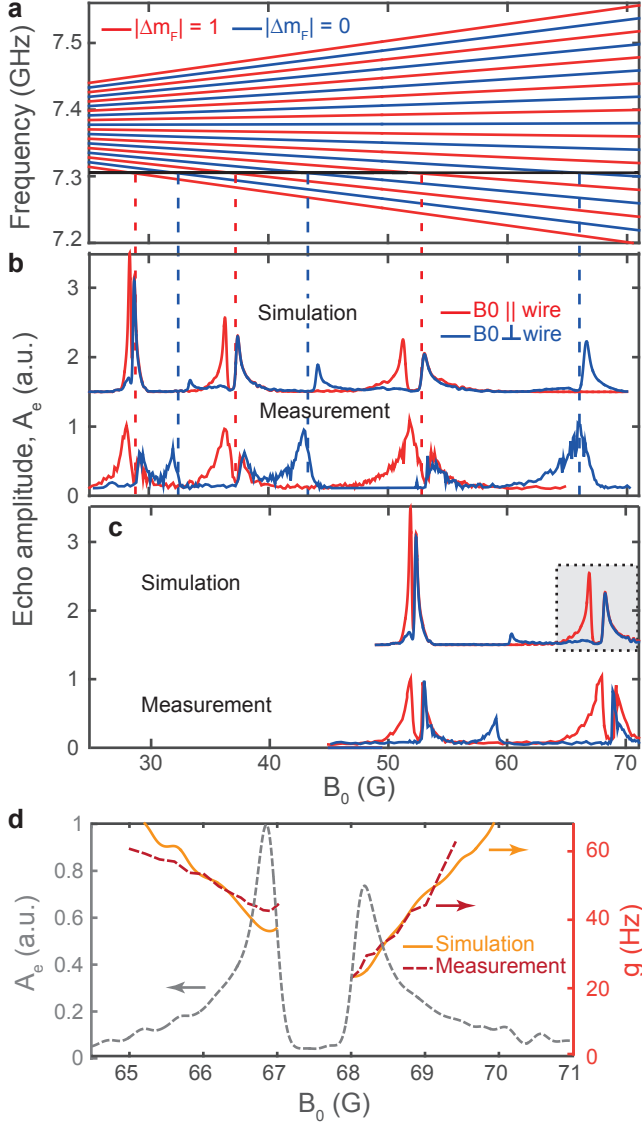


FIG. 4. **a** ESR transition frequencies of the Si:Bi system for $B_0 < 70$ G. Red lines represent the spin transitions that obey the selection rule $\Delta m_F = \pm 1$ (i.e. $\delta B_1 \perp B_0$) whilst the blue lines show $\Delta m_F = 0$ transitions ($\delta B_1 \parallel B_0$). The black solid line indicates the frequency of resonator A ($\omega_{0A}/2\pi = 7.305$ GHz). **b** Compensated echo-detected field sweeps of the first five ESR transitions of resonator A. The bottom traces are measured data, whilst the top traces have been offset intentionally and are the results of our theoretical modeling. **c** Compensated echo-detected field sweeps (measurement and simulation) of the first three ESR transitions of resonator B. **d** The single spin-resonator coupling strength g as a function of field B_0 , extracted on the $|4, -3\rangle \leftrightarrow |5, -4\rangle$ transition of resonator B (marked by the black dashed box in panel c). The red dashed line is derived from measurements of the Rabi frequency and has been offset by 1 G, an amount required to center the measured (not shown) and simulated (grey dashed line) spectra. A qualitative agreement is observed with the simulated data (orange line), which has been scaled so that the two data sets overlap at $B_0 = 68$ G.

erties such as surface roughness and native oxides on the aluminium wire and silicon substrate.

Having successfully reproduced key features of the ESR spectra, we investigate whether our model can also capture the correlation of the spin-resonator coupling g and Larmor frequency, as discussed earlier. The Rabi frequency can be expressed in terms of g and mean intracavity photon number \bar{n} through the relation $\Omega_R = 2g\sqrt{\bar{n}}$. We extract Ω_R as a function of B_0 across the $|4, -3\rangle \leftrightarrow |5, -4\rangle$ transition of resonator B (identified by a black dashed box in Fig. 4c). A calculation of g can then be made by estimating \bar{n} using the experimental input power and a calibration of the loss in our setup [14]. In Fig. 4d we plot the result of the experiment (dark-red dashed line) overlaid on the simulated spectra (grey dashed line). The curve quantifies the qualitative description offered earlier: the coupling strength increases for the spins that are further detuned (those close to the edge of the wire) and reduces towards the center of the transition, reaching the lowest couplings at the inner-edge of the high-field peak (the spins farthest from the wire). Next, we use our model to simulate the expected g versus B_0 dependence, the result is given by the orange solid line in Fig. 4d. The simulated data has been scaled by a factor of 0.7 so that the curve overlaps with the experimental data at $B_0 = 68$ G. We find that all experimental features are qualitatively reproduced, even though the agreement is not fully quantitative. The $\sim 30\%$ discrepancy between simulation and experiment may be explained by uncertainty in the loss calibration (~ 1 dB), together with slight differences between the simulated model and the physical device.

There is just a single unknown parameter in our model, the multiplicative term γ that scales the quadrupole interaction strength in the transformed quadrupole Hamiltonian H'_Q . This parameter incorporates several factors, the most significant being the Sternheimer anti-shielding effect. This phenomenon describes the re-arrangement of the inner electron shells in response to an external EFG, with a resulting enhancement of the total EFG experienced by the nucleus [34]. The Sternheimer enhancement ($1 - \gamma_s$) can be considerable, with $\gamma_s = -47.24$ calculated for Bi^{5+} ions and $\gamma_s = 926.6$ for Bi^{+} ions [39] in isolation. In a silicon crystal, bismuth has four of its valence electrons in covalent bonds, with the fifth only weakly bound to the Coulomb potential of the Bi^{+} donor. It is unknown how the covalent bonding to the silicon lattice should affect γ_s . For a full discussion on other effects that may also be captured by γ , we refer the reader to the Supplementary Material. We found that $\gamma = -900$ (within a range of $\pm 20\%$) provided simulated spectra that most closely resembled the measurements (see Figs. 4b and c). This agrees well with the Sternheimer enhancement expected for Bi^{+} ions of $1 - \gamma_s = -925.6$.

We have presented a technique to study strain in silicon devices through high-sensitivity orientation-dependent

ESR spectroscopy. Our results indicate that strain in micro and nanoelectronic devices plays a considerable part in determining the spin resonance conditions of bismuth donors. We found a large quadrupole interaction resulting from strains inherent to the device — of order 100 MHz for strains of $\sim 10^{-4}$ — leading to an order-of-magnitude broadening of the ESR lines. The level of agreement demonstrated between our finite-element/EMT calculations and the experimental data shows that our model captures the underlying physics. This analysis could be adapted to other device geometries and spin systems, and may prove to be a useful tool for spin-based device design. Furthermore, one can envisage that the signature of quadrupolar splitting in the ESR and NMR spectrum of a single high-spin donor could be used as a very sensitive local probe for strain in nanoelectronic devices. We estimate that with typical intrinsic line-widths achieved for donors in isotopically enriched silicon of ~ 2 kHz [5], a single bismuth donor could be used to measure strains down to 10^{-7} . This could be integrated with other techniques for donor metrology [40] to provide valuable insight into the spatial variation of physical system parameters in nanoscale quantum devices. The results presented in this work have important implications for QIP with donors (in particular those with $I > 1/2$) and in hybrid systems such as superconducting quantum memories.

Acknowledgments We thank P. Mortemousque and D. Franke for fruitful discussions. We acknowledge technical support from N. Panjwani and P. Ross. We acknowledge the support of the European Research Council under the European Community's Seventh Framework Programme (FP7/2007-2013) through grant agreements No. 615767 (CIRQUSS), 279781 (ASCENT) and 630070 (quRAM), and of the Agence Nationale de la Recherche (ANR) through the project QIPSE. J.J.L.M. is supported by the Royal Society. T.S. was supported by the US Department of Energy under contract DE-AC02-05CH11231. F.A.M. and A.M. were supported by the Australian Research Council Discovery Project DP150101863.

* Present Address: Center for Neuroscience and Cognitive Systems, Italian Institute of Technology, Corso Bettini 31 — 38068 Rovereto, Italy

- [1] B. E. Kane, *Nature* **393**, 133 (1998).
- [2] M. Fuechsle, J. A. Miwa, S. Mahapatra, H. Ryu, S. Lee, O. Warschkow, L. C. Hollenberg, G. Klimeck, and M. Y. Simmons, *Nature Nanotechnology* **7**, 242 (2012).
- [3] J. J. Pla, K. Y. Tan, J. P. Dehollain, W. H. Lim, J. J. L. Morton, F. a. Zwanenburg, D. N. Jamieson, A. S. Dzurak, and A. Morello, *Nature* **496**, 334 (2013).
- [4] L. A. Tracy, T.-M. Lu, N. Bishop, G. Ten Eyck, T. Pluym, J. Wendt, M. Lilly, and M. Carroll, *Applied Physics Letters* **103**, 143115 (2013).
- [5] J. T. Muhonen, J. P. Dehollain, A. Laucht, F. E. Hudson, T. Sekiguchi, K. M. Itoh, D. N. Jamieson, J. C. McCallum, A. S. Dzurak, and A. Morello, *Nature Nanotechnology* **9**, 1 (2014).
- [6] A. M. Tyryshkin, S. Tojo, J. J. Morton, H. Riemann, N. V. Abrosimov, P. Becker, H.-J. Pohl, T. Schenkel, M. L. Thewalt, K. M. Itoh, *et al.*, *Nature materials* **11**, 143 (2012).
- [7] K. Saeedi, S. Simmons, J. Z. Salvail, P. Dluhy, H. Riemann, N. V. Abrosimov, P. Becker, H.-J. Pohl, J. J. L. Morton, and M. L. W. Thewalt, *Science* **342**, 830 (2013).
- [8] S. J. Angus, A. J. Ferguson, A. S. Dzurak, and R. G. Clark, *Nano Letters* **7**, 2051 (2007).
- [9] A. Laucht, J. T. Muhonen, F. A. Mohiyaddin, R. Kalra, J. P. Dehollain, S. Freer, F. E. Hudson, M. Veldhorst, R. Rahman, G. Klimeck, *et al.*, *Science Advances* **1**, e1500022 (2015).
- [10] M. H. Mohammady, G. W. Morley, and T. S. Monteiro, *Physical Review Letters* **105**, 2 (2010).
- [11] G. Wolfowicz, A. M. Tyryshkin, R. E. George, H. Riemann, N. V. Abrosimov, P. Becker, H.-J. Pohl, M. L. W. Thewalt, S. a. Lyon, and J. J. L. Morton, *Nature Nanotechnology* **8**, 561 (2013).
- [12] T. Yasukawa, A. J. Sigillito, B. C. Rose, A. M. Tyryshkin, and S. A. Lyon, *Phys. Rev. B* **93**, 121306 (2016).
- [13] A. Bienfait, J. Pla, Y. Kubo, M. Stern, X. Zhou, C. Lo, C. Weis, T. Schenkel, M. Thewalt, D. Vion, *et al.*, *Nature Nanotechnology* **11**, 253 (2015).
- [14] A. Bienfait, J. Pla, Y. Kubo, X. Zhou, M. Stern, C. Lo, C. Weis, T. Schenkel, D. Vion, D. Esteve, *et al.*, *Nature* **531**, 74 (2016).
- [15] J. H. Wesenberg, A. Ardavan, G. a. D. Briggs, J. J. L. Morton, R. J. Schoelkopf, D. I. Schuster, and K. Mølmer, *Physical Review Letters* **103**, 1 (2009).
- [16] Y. Kubo, C. Grezes, A. Dewes, T. Umeda, J. Isoya, H. Sumiya, N. Morishita, H. Abe, S. Onoda, T. Ohshima, V. Jacques, A. Dréau, J. F. Roch, I. Diniz, A. Auffeves, D. Vion, D. Esteve, and P. Bertet, *Physical Review Letters* **107** (2011), 10.1103/PhysRevLett.107.220501.
- [17] B. Julsgaard, C. Grezes, P. Bertet, and K. Mølmer, *Physical Review Letters* **110**, 1 (2013).
- [18] C. Grezes, B. Julsgaard, Y. Kubo, M. Stern, T. Umeda, J. Isoya, H. Sumiya, H. Abe, S. Onoda, T. Ohshima, V. Jacques, J. Esteve, D. Vion, D. Esteve, K. Mølmer, and P. Bertet, *Physical Review X* **4**, 1 (2014).
- [19] P. Mortemousque, S. Rosenius, G. Pica, D. Franke, T. Sekiguchi, A. Truong, M. Vlasenko, L. Vlasenko, M. Brandt, R. Elliman, *et al.*, arXiv preprint arXiv:1506.04028 (2015).
- [20] D. P. Franke, F. M. Hrubesch, M. Künlz, H.-W. Becker, K. M. Itoh, M. Stutzmann, F. Hoehne, L. Dreher, and M. S. Brandt, *Physical Review Letters* **115**, 057601 (2015).
- [21] D. P. Franke, M. P. Pflüger, P.-A. Mortemousque, K. M. Itoh, and M. S. Brandt, *Physical Review B* **93**, 161303 (2016).
- [22] C. Lo, M. Urdampilleta, P. Ross, M. Gonzalez-Zalba, J. Mansir, S. Lyon, M. Thewalt, and J. Morton, *Nature Materials* **14**, 490 (2015).
- [23] T. Thorbeck and N. M. Zimmerman, *AIP Advances* **5**, 087107 (2015).
- [24] *Principles of Superconductive Devices and Circuits* (Prentice Hall PTR, 1999) Chap. 3.
- [25] A. Bienfait, arXiv preprint arXiv:? (2016).
- [26] I. Wisby, S. de Graaf, R. Gwilliam, A. Adamyan, S. Ku-

- batkin, P. Meeson, A. Y. Tzalenchuk, and T. Lindström, arXiv preprint arXiv:1512.02270 (2015).
- [27] A. J. Sigillito, H. Malissa, A. M. Tyryshkin, H. Riemann, N. V. Abrosimov, P. Becker, H.-J. Pohl, M. L. Thewalt, K. M. Itoh, J. J. Morton, *et al.*, Applied Physics Letters **104**, 222407 (2014).
- [28] J. J. Morton, A. M. Tyryshkin, A. Ardavan, K. Porfyrakis, S. Lyon, and G. A. D. Briggs, Physical Review A **71**, 012332 (2005).
- [29] E. Hahn, *Physical Review* **80**, 580 (1950).
- [30] C. D. Weis, C. C. Lo, V. Lang, a. M. Tyryshkin, R. E. George, K. M. Yu, J. Bokor, S. a. Lyon, J. J. L. Morton, and T. Schenkel, *Applied Physics Letters* **100** (2012), 10.1063/1.4704561.
- [31] E. Eiper, R. Resel, C. Eisenmenger-Sittner, M. Hafok, and J. Keckes, Powder Diffraction **19**, 74 (2004).
- [32] M. J. Madou, *Fundamentals of microfabrication: the science of miniaturization* (CRC press, 2002).
- [33] L. Dreher, T. A. Hilker, A. Brandlmaier, S. T. Goennenwein, H. Huebl, M. Stutzmann, and M. S. Brandt, Physical Review Letters **106**, 037601 (2011).
- [34] E. N. Kaufmann and R. J. Vianden, Reviews of Modern Physics **51**, 161 (1979).
- [35] T. Ando, A. B. Fowler, and F. Stern, Reviews of Modern Physics **54**, 437 (1982).
- [36] W. Kohn and J. Luttinger, Physical Review **98**, 915 (1955).
- [37] D. Wilson and G. Feher, Physical Review **124**, 1068 (1961).
- [38] G. Pica, G. Wolfowicz, M. Urdampilleta, M. L. Thewalt, H. Riemann, N. V. Abrosimov, P. Becker, H.-J. Pohl, J. J. Morton, R. Bhatt, *et al.*, Physical Review B **90**, 195204 (2014).
- [39] F. Feiock and W. Johnson, Physical Review **187**, 39 (1969).
- [40] F. A. Mohiyaddin, R. Rahman, R. Kalra, G. Klimeck, L. C. Hollenberg, J. J. Pla, A. S. Dzurak, and A. Morello, Nano Letters **13**, 1903 (2013).